Journal Pre-proof

Defining the molecular landscape of cancer-associated stroma in cutaneous squamous cell carcinoma

Erin Beebe, MSc, Zahra Motamed, MSc, Lennart Opitz, PhD, Phil F. Cheng, PhD, Mitchell P. Levesque, PhD, Enni Markkanen, DVM-PhD, Laurence Feldmeyer, MD-PhD

Please cite this article as: Beebe E, Motamed Z, Opitz L, Cheng PF, Levesque MP, Markkanen E, Feldmeyer L, Defining the molecular landscape of cancer-associated stroma in cutaneous squamous cell carcinoma, *The Journal of Investigative Dermatology* (2022), doi: https://doi.org/10.1016/j.jid.2022.06.017.

Article type: Original article

Title: Defining the molecular landscape of cancer-associated stroma in cutaneous squamous cell carcinoma

Short title: Cancer-associated stroma in squamous cell carcinoma

Erin Beebe, MSc[1], Zahra Motamed[1], MSc, Lennart Opitz, PhD[2], Phil F. Cheng[3], PhD, Mitchell P. Levesque[3], PhD, Enni Markkanen, DVM-PhD[1*], Laurence Feldmeyer, MD-PhD[4*]

[1]Institute of Veterinary Pharmacology and Toxicology, Vetsuisse Faculty, University of Zürich, Winterthurerstr. 260, 8057 Zürich, Switzerland

[2]Functional Genomics Center Zürich, University of Zürich/ETH Zürich, Winterthurerstr. 190, 8057 Zürich, Switzerland

[3]Department of Dermatology, University of Zurich Hospital, University of Zurich, Zurich, Switzerland

[4]Department of Dermatology, Inselspital, Bern University Hospital, University of Bern, Bern, Switzerland

*Shared senior authors.

Corresponding author:

Laurence Feldmeyer, MD-PhD

Department of Dermatology

Inselspital, Bern University Hospital

University of Bern

3010 Bern

Switzerland

Email: laurence.feldmeyer@insel.ch

IRB approval status: Reviewed and approved by the ethics committee of the Canton of Bern (KEK-2018-02207).

Reprint requests: Laurence Feldmeyer

Manuscript word count: 3472 words [excluding abstract, references, figures, tables]

Abstract word count: 199

References: 41

Figures: 5

Supplementary figures: 3

Tables: 1

Supplementary tables: 7

Attachments: CONSORT checklist, research protocol

Abbreviations: ANGPTL1: angiopoietin like 1, AK: actinic keratosis; CAF: cancer associated fibroblasts, CAS: cancer-associated stroma, cSCC: cutaneous squamous cell carcinoma,

CXCL13: C-X-C motif chemokine ligand 13, ECM: extracellular matrix, EGFR: epidermal growth factor receptor, FDR: false discovery rate, FFPE: formalin-fixed paraffin embedded, GEDIT: Gene Expression Deconvolution Interactive Tool, GSEA: gene set enrichment analysis, GSN: gelsolin, IL-6: interleukin-6, LCM: laser-capture microdissection, lncRNA: long non coding RNA, MMP1 matrix metalloproteinase 1, PCA: principal component analysis, PD-1: programmed death-1, PNI: perineural infiltration, RNAseq: RNA sequencing, ROI: region of interest, S100A8: S100 calcium binding protein A8, TIMP3: tissue metalloproteinase inhibitor 3, TME: tumor microenvironment, UV: ultraviolet.

Keywords: cutaneous squamous cell carcinoma, tumor stroma, tumor microenvironment, formalin-fixed paraffin embedded, RNAseq, laser-capture microdissection

Abstract

Cutaneous squamous cell carcinoma (cSCC) is the 2nd most common skin cancer world-wide. Cancer-associated stroma (CAS) is central to tumor development and strongly influences therapy response. Perineural infiltration (PNI) represents a major risk factor for cSCC and likely influences CAS reprogramming. However, stromal reprogramming in cSCC remains poorly characterized, and it is unknown whether and how PNI influences CAS. To address these questions, we analyzed CAS and matched normal stroma from 20 cSCC cases (11 without and 9 with PNI) by laser-capture microdissection (LCM) using RNA-sequencing. Our analysis reveals extensive stromal reprogramming strongly driven by changes in immune cells, as validated using immunohistochemistry. Furthermore, CAS of cSCC displays markers of immune exhaustion, and multiplex spatial analysis suggests PD-L1 expression on NK-T cells contributes to T cell exhaustion and immunosuppression. Finally, PNI is characterized by increased IL-17A. In PNI negative cases, IL-17A derives predominantly from CD3+ cells. With PNI however, we observe an increased contribution of fibroblasts to high IL-17A, which coincides with a significant increase in FAP+ cells. Our analysis elucidates the molecular landscape of CAS in cSCC and identifies the presence of immunosuppressive mechanisms, supporting further research into immunotherapy and anti-IL-17A in cSCC especially for cases with PNI.

INTRODUCTION

Cutaneous squamous cell carcinoma (cSCC) is the 2nd most common skin cancer world-wide, with over 700'000 new cases per year in the United States. Cancer-associated stroma (CAS), composed of infiltrating immune cells, fibroblasts, vascular cells and others, strongly influences tumor initiation, progression and therapy response (Bissell and Hines 2011; Hanahan and Coussens 2012). To date however, with only one study reporting on CAS of 10 cSCC cases available (Ji et al. 2020), specific analyses of changes differentiating CAS from normal stroma in cSCC are exceedingly sparse. Moreover, perineural infiltration (PNI) represents one of the most important risk factors for cSCC aggressiveness and is associated with poor prognosis, high local recurrence and frequent nodal metastasis in cSCC (Haug et al. 2020). Given the strong influence of CAS on tumor malignancy, stromal reprogramming is likely to differ according to the PNI status of tumors. Nevertheless, it remains unknown whether and how CAS changes in relation to PNI.

While locally invasive cSCC can be treated by surgical excision and/or radiotherapy, management of locally advanced or metastatic cSCC requires specific therapy and an established consensus on first-line systemic treatment. Immunotherapy with immune checkpoint programmed death-1 (PD-1) inhibitors recently received FDA approval for use in advanced cSCC (Fitzgerald and Tsai 2019) and are expected to become the next gold-standard treatment for patients with locally advanced and metastatic cSCC (Benzaquen 2020). Whether this therapy might also benefit patients with PNI positive tumors remains unanswered. Improved understanding of CAS reprogramming in cSCC has the potential to stratify patients for better

therapy response and identify potential novel stromal drivers of the disease.

RESULTS

RNAseq-based transcriptomic profiling of matched cancer-associated and normal stroma from cSCC isolated by LCM from FFPE specimens

To characterize stromal changes in cSCC, we analyzed CAS and matched normal stroma of 20 cSCC clinical FFPE cases using RNAseq. Detailed patient characteristics can be found in Table 1. Principal component analysis (PCA) revealed clear differences between CAS and normal stroma, demonstrating that CAS in cSCC undergoes strong reprogramming (Fig. 1a). Differential gene expression analysis (p-value < 0.01, FC > 2) revealed 800 genes (472 upregulated, 328 downregulated) to be significantly deregulated in CAS compared to normal stroma (Fig. 1b) (Supplementary Tables S1 and S2). Association of significantly deregulated genes with the top over-represented GO terms revealed downregulated genes to participate in cell adhesion (cluster 4) as well as metabolism and ion homeostasis (cluster 1), and upregulated genes to play a role in immune system processes (clusters 2,3,6) and organization of the extracellular matrix (cluster 5) (Fig. 1c). Accordingly, hypergeometric overrepresentation of the biological processes associated with strongly up-regulated genes in CAS revealed enrichment of immune-related responses including innate and adaptive immune responses (Fig. 1d), while down-regulated genes showed enrichment for developmental pathways (Fig. 1e).

Successful validation using RT-qPCR was performed for seven of the most significantly differentially expressed genes; ANGPTL1 (angiopoietin like 1), GSN (gelsolin), TIMP3

(metalloproteinase inhibitor 3), IL-6 (interleukin-6), S100A8 (S100 calcium binding protein A8),

CXCL13 (C-X-C motif chemokine ligand 13) and MMP1 (matrix metalloproteinase 1) (Fig. 2).

CAS in cSCC is characterized by strong changes in immune cell infiltration and displays

signs of immune exhaustion

To determine factors differentiating normal stroma and CAS, we performed gene set enrichment

analysis (GSEA) of our dataset using WebGestalt (Liao et al. 2019). Kegg pathway analysis of

the significantly deregulated targets revealed enrichment of IL-17, TNF and NF-kappa B

signaling in CAS (Fig. 3a). These findings were verified through REACTOME pathway analysis

which demonstrated a significant enrichment of multiple immune-system related pathways (Fig.

3b). Given that stroma is a mixture of different cell types that can vary in abundance between

CAS and normal stroma, we next asked how the cellular composition changed between disease

states. To assess this, we utilized the Microenvironment Cell Populations-counter (MCP-counter,

Becht et al. 2016). As expected, sample content was dominated by fibroblasts (Fig. 3c).

Comparison of cellular composition revealed significant increases in T cells (p = 0.0184), CD8 T

cells (p = 0.0014), B cells (p = 0.0069) and NK cells (p = 0.0194) and a corresponding decrease

in fibroblasts (p = 0.0116) in CAS compared to normal stroma. To aid estimation of immune cell

content, we repeated analysis using the gene expression deconvolution interactive tool (GEDIT)

(Nadel et al. 2021) (applying the LM22 (Newman et al. 2015) and human skin signatures

(Swindell et al. 2013) as reference matrices) (Fig. 3d). This revealed significant increases in

naïve and memory B cells, resting NK cells, activated CD4 memory T cells, M1-polarized

macrophages, activated dendritic cells and CD8 T cells. Conversely, resting mast cells were

significantly decreased in CAS compared to normal stroma. Supporting analysis using

CIBERSORTx (Newman et al. 2019) further corroborated these results (Fig. 3e). Other detected immune cell populations either did not differ significantly in abundance between CAS and normal stroma or yielded conflicting evidence between the deconvolution tools. Immunohistochemistry validated changes in stromal immune infiltration (Fig. 4).

Characterization of gene expression according to specific immune modules highlighted significant upregulation of PD-L1 (CD274), IDO1 and LGALS9, which have been shown to promote immunosuppression (Fig. 3f). At the same time, we observed a significant increase in the T cell inhibition and exhaustion markers LAG3, TIGIT, PD-1, CTLA-4, BTLA, KLRC1 and LAYN. In addition, increased expression in cytotoxic effector molecules including GZMA, GZMB and IFNG as well as co-stimulatory molecules such as CD28 and ICOS was observed.

CAS from tumors with PNI is characterized by increased IL-17 signaling and immunosuppression

To further our understanding of the mechanisms driving PNI, differential expression analysis (p-value < 0.5, FC > 2) of PNI positive (n=9) and negative (n=11) cases (Table 1) revealed 340 significantly deregulated genes (176 upregulated, 164 downregulated) (Fig. 5a, Supplementary Tables S3 and S4). Significantly upregulated genes identified included MUC4, ACTA1 and multiple immunoglobulins (IGKV2-28, IGLV-19, IGKV1-33). Interestingly, we also detected significant upregulation of the lncRNA, MIR633-AHG. Over-representation analysis of Gene Ontology (GO) terms suggested the strongest changes in the following categories: immune system process, regulation of cell proliferation and muscle development and function among the upregulated genes and ECM organization and apoptosis among the downregulated genes (Fig. 5b).

Multiplex immunohistochemistry was employed to further investigate differences in immune response according to PNI status and to assess the potential contribution of cell types to IL-17 signaling (Fig. 3a). We performed spatial expression analysis of a subset of interesting markers (CD3, CD163, CD56, FAP, IL-17A and PD-L1) using PerkinElmer Vectra® Polaris™ multiplex imaging system in 9 cSCC cases (4 negative, 5 positive, Table 1). In brief, multiple regions of interest (ROI) were selected per tissue section corresponding to regions of CAS isolated with LCM (Supplementary Figure S2). Across 89 ROI, a total of 137,424 stromal cells (61,232 in PNI negative and 76,192 in PNI positive cases) were identified and used for downstream analysis (Supplementary Figure S3a, Supplementary Table S7). Quantification of inForm cell segmentation summary data identified significant differences between PNI positive and negative cases, including significant increases in IL-17A+ and FAP+ populations and significant decreases in PD-L1+ and CD163+ populations (Fig. 5c). In-depth co-expression analysis was performed using Giotto (version 2.0.0.957, Dries et al 2021). UMAP clustering of all cells from all samples confirmed patient and PNI status heterogeneity (Supplementary Figures S3c and S3d). 7 key cell phenotypes were identified, namely CD163+ (macrophages), FAP+ (fibroblasts), a subpopulation of FAP+ cells co-expressing IL-17A, CD3+ (T cells), a subpopulation of CD3+ cells co-expressing IL-17A and an interesting population characterized by CD3+/ CD56+/ PD-L1+ (NK-T cells) also co-expressing IL-17A+ (Figs. 5d and e). Phenotypes were merged according to key cell types CD163, CD3 and FAP (Fig. 5f). Notably, IL-17A expression was concurrent with both FAP and CD3 populations (Fig. 5f). To further explore the source of increased IL-17A, distribution of the top 25% of signal (IL-17 high) was inspected, confirming CD3+ cells as the dominant contributors of IL-17A expression. Of interest however, IL-17A

expression was not limited to T cells and was also observed on NK-T cells and fibroblasts (Fig. 5g). While CD3-derived IL-17A remained dominant, a marked increase in fibroblast-derived IL-17A was observed in PNI positive cases (p-value = 0.063) (Fig. 5g, Supplementary Figure S3e). The presence of co-expressing cell populations was confirmed by observation (Fig. 5h).

DISCUSSION

Using transcriptomic analysis coupled with validation via RT-qPCR, we report significant downregulation of ANGPTL1, GSN and TIMP3 and upregulation of IL-6, S100A8, CXCL13 and MMP1 in CAS compared to normal stroma, all of which are known to have important functions in CAS. IL-17 signaling was identified as significantly enriched in CAS over normal stroma according to KEGG pathway analysis, while REACTOME detected significant enrichment for a diverse range of immune pathways (Fig. 3). Deconvolution using MCP-counter, GEDIT and CIBERSORTx facilitated comparative analysis of immune cell populations in CAS and normal stroma leading to the identification of significant differences in B cell, NK cell, CD4+ and CD8+ T cell, M1 macrophage, dendritic and mast cell populations that could be validated by IHC (Fig. 4). Furthermore, analysis of expression patterns across patient-matched tissue revealed significant upregulation in representative immune modules, including markers for immune suppression and exhaustion (Fig. 3f). These data provide a clinically relevant insight to the extent of stromal reprogramming dependent on immune cells and fully supports further research into the use of immunotherapy for cSCC patients.

PNI is a high-risk factor in the prognosis of primary cutaneous SCC and is associated with lymph node metastasis, recurrence and tumor-specific death (Haug et al. 2020). To our knowledge, we

detail previously unreported differences in stromal reprogramming between cases with and without PNI. Analysis of CAS according to PNI status revealed a strong upregulation of several immunoglobulin variants, hinting at the enrichment for immune system processes (Fig. 5a). The most strongly upregulated target was MUC4, a membrane-bound mucin that promotes carcinogenic progression particularly due to its signaling and anti-adhesive properties. MUC4 is expressed on respiratory epithelial cells, but also in smooth muscle cells and adipose tissue (Proteinatlas). MUC4 has previously been described as a marker of poor prognosis for pancreatic, colon and stomach cancers (Jonckheere and Van Seuningen 2018). Interestingly, we also detected significant upregulation of lncRNA, MIR663AHG. While little is known about the specific function of MIR663AHG, lncRNAs in cancer are an emerging field of research. It is therefore an advantage that, using this technique, we can detect differences in expression patterns of different types of RNA.

Multiplex immunohistochemistry revealed CAS from PNI positive tumors could be further characterized by an overall increase in IL-17A+ stromal cells, as previously reported in systemic sclerosis (Nakashima et al. 2012). IL-17 has been shown to promote development of prostate, colon, nonmelanoma skin, lung, breast, and pancreatic cancer, and IL-17 and IL-22 promoted tumor progression in cSCC cell lines (Nardinocchi et al. 2015). This cytokine could present an interesting target for aggressive cSCC, as IL-17 inhibitor agents (secukinumab, ixekizumab, and brodalumab) are currently available on the market for the treatment of psoriasis. A role of IL-17 in tumor stroma has already been demonstrated in other cancer types like oropharyngeal SCC (Punt et al. 2017), oral SCC (Avadhani et al. 2017), pancreatic cancer (Mucciolo et al. 2021) and colorectal adeno-carcinoma (Cui et al. 2021), and secukinumab combined with IL-35 reduced the invasive migration capability of hepatoma cells (Li et al. 2016). We identified T cells, NK-T

cells and fibroblasts as sources of IL-17A. As expected , CD3+ cell populations emerged as the

dominant source of IL-17A in both PNI negative and positive cases (Fig. 5g-h) (McGeachy et al.

2019; Rachitskaya et al. 2008; Yu et al. 2017).

PNI positive cases displayed a significant increase in FAP+ cells (Fig. 5c) and an increase in

FAP+ contribution to IL-17A signal (Fig. 5g). It is widely known that fibroblasts express IL-

17RA receptors (Hwang et al. 2004) thus are key effectors of downstream IL-17 signaling, for

example leading to increased IL-6 and IL-8 secretion (Fossiez et al. 1996). However, it has also

been shown that IL-17 was overexpressed in colorectal CAFs following chemotherapy, leading

to the onset of chemoresistance through stromal remodeling (Lotti et al. 2013). With this

knowledge, the potential importance of targeting IL-17 prior to chemotherapy, or alternative

therapeutic strategies, should be highlighted to avoid development of possible therapeutic

resistance induced by fibroblast activation. Furthermore, it is interesting to note that CAFs have

been shown to inhibit the cytotoxic activity of NK cells (Inoue et al. 2016; Zhang et al. 2019)

and to exhibit further immunosuppressive functions (Mhaidly and Mechta-Grigoriou 2020).

In line with immune suppression, we identify a concomitant decrease in PD-L1+ cells in CAS

from PNI positive compared to PNI negative cases. Strong clustering suggests direct co-

expression of PD-L1 on NK-T cells in our dataset (Fig. 5e). This diverges from a recent report

suggesting migrating dendritic cells (DCs) to be a major source of PD-L1 in cSCC (Ji et al.

2020). PD-L1 expression on NK-T cells presents a largely understudied phenomenon that has

been shown to limit T cell activation by promoting self-tolerance and suppressing neighboring

macrophages and effector T cells in tumors, to drive them into apoptosis or to adopt a regulatory

phenotype. Hence, presence of PD-L1 on T cells seems to support immune suppression and

facilitates tumorigenesis (Diskin et al. 2020; Fanelli et al. 2021). Based on this, we hypothesize that PD-L1 expression on NK-T cells could contribute to their exhaustion and apoptosis in PNI positive cases, in line with a trend towards a decrease in CD3+ cells, suggesting a diminished NK-T cell population (Fig. 5c). Given the immune-suppressive effects of CAFs discussed above, a potential role for CAFs in contributing to this loss of PD-L1 expressing cells in PNI positive cases seems possible. Finally, engagement of PD-L1 expressed on T cells has been shown to weaken antitumor immunity not only by suppressing T-effector cells but also macrophages in the tumor microenvironment (Diskin et al. 2020). This is in accordance with a significant decrease in CD163+ macrophages in PNI positive cases (Fig. 5c).

In parallel, NK-T cells (CD3+, CD56+) act at the interface of adaptive and innate immunity. We can hypothesize that given the immunosuppressive state induced by direct expression of PD-L1 on NK-T cells, the NK-T population observed in this study is that of an anergic immunosuppressive T_H2-like subset with the potential to promote tumor progression (Krijgsman et al. 2018). Interestingly, increased levels of IL-17A, as discussed above, have also been associated with inhibiting maturation of NK cells thus contributing to tumor development through the initiation of an immunosuppressive microenvironment (Wang et al. 2019). Finally, to acknowledge inherent limitations, while our multiplex IHC analysis cannot fully deconvolute all cells present in CAS due to technical limitations, we are convinced of the value of these insights into CAS reprogramming between PNI positive and negative cSCC cases.

Together, these data identify simultaneous yet independent mechanisms driving immunosuppression in PNI positive cSCC: an increase in IL-17A expression by NK-T cells and PD-L1-engagement driven suppression of T cells and macrophages. Indeed, although no clinical

trial investigated yet anti PD-1 or anti PD-L1 in perineural disease, These data provide rationale for further drug response studies with the hypothesis that patients with PNI might respond well to PD-1/PD-L1 inhibition and anti-IL-17A therapy, such as secukinumab, currently approved for treatment of psoriasis (von Stebut et al. 2020; Wasilewska et al. 2016).

In summary, we provide a proof-of-principle to analyze specifically the tumor stroma in clinical FFPE tissue isolated through LCM by RNAseq and refine our understanding of the factors involved in the microenvironment that have potential to inform clinical decision-making. We were able to systematically analyze gene expression in the stroma of cSCC, while so far, most literature on cSCC has not differentiated clearly between the tumor and its environment. RNA isolation in routine histological samples opens an unexplored field with unlimited possibilities, without requirement of snap frozen biopsies. Our analyses allow defining a "molecular landscape" of CAS-specific gene-expression in cSCC and a better understanding of factors influencing cSCC progression and field cancerization.

MATERIALS AND METHODS

Case selection. 20 FFPE tissue blocks of cSCC samples were obtained from the Department of Dermatology, Inselspital, Bern (written, informed consent available) (Table 1). Criteria for case selection included immunocompetent patients, an excision specimen of a previously punch-biopsied moderately differentiated cSCC, and sufficient tumor stroma content for tissue isolation. All cases were reviewed by a certified dermatopathologist (LF) for presence or absence of PNI as identified in Supplementary Figure S1.

Laser-capture microdissection (LCM). Tissue processing and selective isolation of matched CAS and normal stroma was performed as previously described using the ArcturusXT^{TM} Laser Capture Microdissection System (Thermo Scientific) as outlined in (Amini et al. 2019; Amini et al. 2017; Ettlin et al. 2017). For further detail see Supplementary Methods.

RNA isolation and sequencing. RNA was isolated from LCM samples as described in (Amini et al. 2017). Details about RNA concentration, yield, and quality can be found in Supplementary Table S5. 10 ng of RNA was submitted for RNAsequencing and analyzed as outlined in (Amini et al. 2019). RNAsequencing was performed in 2 cohorts: cases 25-30 were included as a second cohort including 1 PNI positive and 1 PNI negative from the first cohort in the sequencing run to remove batch effects in the final analysis.

Bioinformatics analyses. The raw reads were cleaned by removing adapter sequences, trimming low quality ends, and filtering reads with low quality (phred quality <20) using Trimmomatic (Version 0.36) (Bolger et al. 2014). Sequence pseudoalignment of the resulting high-quality reads to the Human reference genome (build GRCh38.p13; gene model definitions based on GENCODE r32) and quantification of gene level expression was carried out using Kallisto (Version 0.44)(Bray et al. 2016). Gene counts were imported into the R/Bioconductor package EdgeR (Robinson et al. 2010) (R version: 3.6.1, EdgeR version: 3.28) and TMM normalization size factors were calculated to adjust for samples for differences in library size. The generalized linear model was used to detect differentially expressed genes incorporating adjusted (Benjamini and Hochberg method) p-values.

Quantitative RT-PCR. Quantitative RT-PCR using Taqman primers (Supplementary Table S6) was performed as described in (Amini et al. 2017) using 6 of the cSCC cases.

Estimation of cell proportions. Quantitation of cell proportions based on RNAseq normalized counts was performed using the MCP-counter (Becht et al. 2016), GEDIT (Nadel et al. 2021) with reference matrices "LM22" and "skin signatures" and CIBERSORTx (Newman et al. 2019).

Immunohistochemistry. Immunohistochemical analysis using the avidin-biotin complex-alkaline phosphatase (ABC-AP) method was performed with following primary antibodies: CD4 (clone 4B12, DakoCytomation), CD8 (clone 4B11, Leica Biosystems), CD138 (clone MI15, Leica Biosystems), CD20 (clone L26, Leica Biosystems), CD117 (clone T595, Leica Biosystems), CD68 (clone PG-M1, DakoCytomation), PD-1 (clone CAL20, Leica Biosystems). Irrelevant immunoglobulin G subclass-matched antibodies were used for negative controls.

Multiplex immunohistochemistry. BOND RXm fully automated staining system was used in conjunction with the Opal Polaris 7-Color Automated IHC Detection Kit (Akoya Biosciences, NEL871001KT) according to user manual instructions. All antibodies were used at a dilution 1:100 (IL-17A (Abcam, ab79056), PD-L1 (Cell Signaling, E1L3N®), CD56 (Abcam, ab220360), CD3 (Dako, AG0452), FAP (Abcam, ab227703) and CD163 (Abcam, ab182422)). Slides were imaged simultaneously using the PerkinElmer Vectra® Polaris™ imaging system maintained by the Center for microscopy and image analysis, University of Zurich.

Slide visualization and ROI selection was performed in Phenochart™ whole slide viewer (Akoya Biosciences).Whole slide scans can be made available upon reasonable request. Tissue was annotated according to tumor or stromal tissue. Cell segmentation training was performed according to DAPI nuclear staining followed by cell marker phenotyping (CD3, CD163, CD56, FAP, IL-17A and PD-L1) (Supplementary Figure S2). Cell segmentation summary data was plotted for each ROI and summarized for each patient sample (Fig. 5c). In-depth spatial

expression analysis was performed using Giotto (version 2.0.0.957, (Dries et al. 2021). Cell

metadata available in Supplementary Table S7. For further detail see Supplementary Methods.

Data Availability Statement

The raw and processed data from RNAsequencing are available at the European Nucleotide

Archive (ENA; accession number PRJEB45432). All supporting data is contained in the

manuscript and in the Supplementary figures and tables. Whole slide scans from multiplex

immunohistochemistry can be made available upon reasonable request.

ORCiDs

Erin Beebe: http://orcid.org/0000-0002-3947-3900

Zahra Motamed: https://orcid.org/0000-0002-0538-2170

Lennart Opitz: http://orcid.org/0000-0001-7945-6737

Phil Cheng: https://orcid.org/0000-0003-2940-006X

Mitchell P. Levesque: https://orcid.org/0000-0001-5902-9420

Enni Markkanen: http://orcid.org/0000-0001-7780-8233

Laurence Feldmeyer: http://orcid.org/0000-0002-4858-5525

CONFLICT OF INTEREST

The authors declare that they have no conflict of interest.

AUTHOR CONTRIBUTIONS

Conceptualization: EM, LF; Data Curation: EB, EM, LF, ZM, LO, PC; Resources: EM, LF, ML, Software: LO, EB, PC, Formal Analysis: EB, EM, LF, ZM, LO, PC; Project Administration: EM, LF; Supervision: EM, LF; Writing of the original Draft: EB, EM, LF; Writing the Review and Editing: EB, EM, LF, ZM, PC.

References

Amini P, Ettlin J, Opitz L, Clementi E, Malbon A, Markkanen E. An optimised protocol for isolation of RNA from small sections of laser-capture microdissected FFPE tissue amenable for next-generation sequencing. BMC Mol. Biol. 2017;18(1):22

Amini P, Nassiri S, Ettlin J, Malbon A, Markkanen E. Next-generation RNA sequencing of FFPE subsections reveals highly conserved stromal reprogramming between canine and human mammary carcinoma. Disease Models & Mechanisms. 2019;12(8)

Avadhani AV, Parachuru VPB, Milne T, Seymour GJ, Rich AM. Multiple cells express interleukin 17 in oral squamous cell carcinoma. J Oral Pathol Med. 2017;46(1):39–45

Becht E, Giraldo NA, Lacroix L, Buttard B, Elarouci N, Petitprez F, et al. Estimating the population abundance of tissue-infiltrating immune and stromal cell populations using gene expression. Genome Biol. 2016;17(1):218

Benzaquen M. Update on the anti-programmed cell death-1 receptor antibodies in advanced cutaneous squamous-cell carcinoma. Dermatol Ther. 2020;33(3):e13325

Bissell MJ, Hines WC. Why don't we get more cancer? A proposed role of the microenvironment in restraining cancer progression. Nat. Med. 2011;17(3):320–9

Bolger AM, Lohse M, Usadel B. Trimmomatic: a flexible trimmer for Illumina sequence data. Bioinformatics. 2014;30(15):2114–20

Bray NL, Pimentel H, Melsted P, Pachter L. Near-optimal probabilistic RNA-seq quantification. Nat Biotechnol. 2016;34(5):525–7

Cui G, Li Z, Florholmen J, Goll R. Dynamic stromal cellular reaction throughout human colorectal adenoma-carcinoma sequence: A role of TH17/IL-17A. Biomed Pharmacother. 2021;140:111761

Diskin B, Adam S, Cassini MF, Sanchez G, Liria M, Aykut B, et al. PD-L1 engagement on T cells promotes self-tolerance and suppression of neighboring macrophages and effector T cells in cancer. Nat Immunol. 2020;21(4):442–54

Ettlin J, Clementi E, Amini P, Malbon A, Markkanen E. Analysis of Gene Expression Signatures in Cancer-Associated Stroma from Canine Mammary Tumours Reveals Molecular Homology to Human Breast Carcinomas. Int J Mol Sci. 2017;18(5)

Fanelli G, Romano M, Nova-Lamperti E, Werner Sunderland M, Nerviani A, Scottà C, et al. PD-L1 signaling on human memory CD4+ T cells induces a regulatory phenotype. PLoS Biol. 2021;19(4):e3001199

Fitzgerald K, Tsai KK. Systemic therapy for advanced cutaneous squamous cell carcinoma. Semin Cutan Med Surg. 2019;38(1):E67–74

Fossiez F, Djossou O, Chomarat P, Flores-Romo L, Ait-Yahia S, Maat C, et al. T cell interleukin-17 induces stromal cells to produce proinflammatory and hematopoietic cytokines. J Exp Med. 1996;183(6):2593–603

Hanahan D, Coussens LM. Accessories to the crime: functions of cells recruited to the tumor microenvironment. Cancer Cell. 2012;21(3):309–22

Haug K, Breuninger H, Metzler G, Eigentler T, Eichner M, Häfner H-M, et al. Prognostic Impact of Perineural Invasion in Cutaneous Squamous Cell Carcinoma: Results of a Prospective Study of 1,399 Tumors. J Invest Dermatol. 2020;140(10):1968–75

Hwang S-Y, Kim J-Y, Kim K-W, Park M-K, Moon Y, Kim W-U, et al. IL-17 induces production of IL-6 and IL-8 in rheumatoid arthritis synovial fibroblasts via NF-κB- and PI3-kinase/Akt-dependent pathways. Arthritis Res Ther. 2004;6(2):R120

Inoue T, Adachi K, Kawana K, Taguchi A, Nagamatsu T, Fujimoto A, et al. Cancer-associated fibroblast suppresses killing activity of natural killer cells through downregulation of poliovirus receptor (PVR/CD155), a ligand of activating NK receptor. Int J Oncol. 2016;49(4):1297–304

Ji AL, Rubin AJ, Thrane K, Jiang S, Reynolds DL, Meyers RM, et al. Multimodal Analysis of Composition and Spatial Architecture in Human Squamous Cell Carcinoma. Cell. 2020;182(6):1661–2

Jonckheere N, Van Seuningen I. Integrative analysis of the cancer genome atlas and cancer cell lines encyclopedia large-scale genomic databases: MUC4/MUC16/MUC20 signature is associated with poor survival in human carcinomas. J Transl Med. 2018;16(1):259

Krijgsman D, Hokland M, Kuppen PJK. The Role of Natural Killer T Cells in Cancer—A Phenotypical and Functional Approach. Frontiers in Immunology. 2018;9 Available from: https://www.frontiersin.org/article/10.3389/fimmu.2018.00367

Li HC, Zhang YX, Liu Y, Wang QS. Effect of IL-17 monoclonal antibody Secukinumab combined with IL-35 blockade of Notch signaling pathway on the invasive capability of hepatoma cells. Genet Mol Res. 2016;15(2)

Liao Y, Wang J, Jaehnig EJ, Shi Z, Zhang B. WebGestalt 2019: gene set analysis toolkit with revamped UIs and APIs. Nucleic Acids Res. 2019;47(W1):W199–205

Lotti F, Jarrar AM, Pai RK, Hitomi M, Lathia J, Mace A, et al. Chemotherapy activates cancer-associated fibroblasts to maintain colorectal cancer-initiating cells by IL-17A. J Exp Med. 2013;210(13):2851–72

McGeachy MJ, Cua DJ, Gaffen SL. The IL-17 Family of Cytokines in Health and Disease. Immunity. 2019;50(4):892–906

Mhaidly R, Mechta-Grigoriou F. Fibroblast heterogeneity in tumor micro-environment: Role in immunosuppression and new therapies. Semin Immunol. 2020;48:101417

Mucciolo G, Curcio C, Roux C, Li WY, Capello M, Curto R, et al. IL17A critically shapes the transcriptional program of fibroblasts in pancreatic cancer and switches on their protumorigenic functions. Proc Natl Acad Sci U S A. 2021;118(6):e2020395118

Nadel BB, Lopez D, Montoya DJ, Ma F, Waddel H, Khan MM, et al. The Gene Expression Deconvolution Interactive Tool (GEDIT): accurate cell type quantification from gene expression data. Gigascience. 2021;10(2)

Nakashima T, Jinnin M, Yamane K, Honda N, Kajihara I, Makino T, et al. Impaired IL-17 signaling pathway contributes to the increased collagen expression in scleroderma fibroblasts. J Immunol. 2012;188(8):3573–83

Nardinocchi L, Sonego G, Passarelli F, Avitabile S, Scarponi C, Failla CM, et al. Interleukin-17 and interleukin-22 promote tumor progression in human nonmelanoma skin cancer. Eur J Immunol. 2015;45(3):922–31

Newman AM, Liu CL, Green MR, Gentles AJ, Feng W, Xu Y, et al. Robust enumeration of cell subsets from tissue expression profiles. Nat Methods. 2015;12(5):453–7

Newman AM, Steen CB, Liu CL, Gentles AJ, Chaudhuri AA, Scherer F, et al. Determining cell type abundance and expression from bulk tissues with digital cytometry. Nat Biotechnol. 2019;37(7):773–82

Punt S, Baatenburg de Jong RJ, Jordanova ES. Four-color Fluorescence Immunohistochemistry of T-cell Subpopulations in Archival Formalin-fixed, Paraffin-embedded Human Oropharyngeal Squamous Cell Carcinoma Samples. J Vis Exp. 2017;(125)

Rachitskaya AV, Hansen AM, Horai R, Li Z, Villasmil R, Luger D, et al. Cutting Edge: NKT Cells Constitutively Express IL-23 Receptor and RORγt and Rapidly Produce IL-17 upon Receptor Ligation in an IL-6-Independent Fashion. J Immunol. 2008;180(8):5167–71

Robinson MD, McCarthy DJ, Smyth GK. edgeR: a Bioconductor package for differential expression analysis of digital gene expression data. Bioinformatics. 2010;26(1):139–40

von Stebut E, Boehncke W-H, Ghoreschi K, Gori T, Kaya Z, Thaci D, et al. IL-17A in Psoriasis and Beyond: Cardiovascular and Metabolic Implications. Front Immunol. 2020;10:3096

Swindell WR, Johnston A, Voorhees JJ, Elder JT, Gudjonsson JE. Dissecting the psoriasis transcriptome: inflammatory- and cytokine-driven gene expression in lesions from 163 patients. BMC Genomics. 2013;14:527

Wang X, Sun R, Hao X, Lian Z-X, Wei H, Tian Z. IL-17 constrains natural killer cell activity by restraining IL-15–driven cell maturation via SOCS3. Proc Natl Acad Sci U S A. 2019;116(35):17409–18

Wasilewska A, Winiarska M, Olszewska M, Rudnicka L. Interleukin-17 inhibitors. A new era in treatment of psoriasis and other skin diseases. Postepy Dermatol Alergol. 2016;33(4):247–52

22

Yu J-S, Hamada M, Ohtsuka S, Yoh K, Takahashi S, Miaw S-C. Differentiation of IL-17-Producing Invariant Natural Killer T Cells Requires Expression of the Transcription Factor c-Maf. Front Immunol. 2017;8:1399

Zhang R, Qi F, Zhao F, Li G, Shao S, Zhang X, et al. Cancer-associated fibroblasts enhance tumor-associated macrophages enrichment and suppress NK cells function in colorectal cancer. Cell Death Dis. 2019;10(4):273

Table legend

Table 1. Overview of cSCC cases included in this study. Clinical data of patients with cSCC.

Case # = case number as referred to within this study. Age = age of patient at excision of tumor.

PNI indicates the presence or absence of histologically confirmed perineural infiltration.

Histological tumor thickness in millimeter. AK indicates the presence or absence of actinic

keratosis. RT-qPCR indicates the cases that were used for validation of expression changes by

RT-qPCR. Multiplex IHC indicates cases selected for spatial expression analysis.

Case # (n=20)	Gender	Age (years)	PNI	Tumor thickness (mm)	AK	RT-qPCR (n=6)	Multiplex IHC (n=9)
1	m	67	Negative	4	Positive	x	x
2	m	72	Positive	8	Positive	x	x
3	m	70	Positive	7	Positive		x
4	m	69	Negative	2	Negative		x
5	m	66	Negative	1.7	Positive	x	
7	m	73	Negative	8.5	Negative	x	
10	m	76	Positive	6	Negative	x	
11	m	78	Negative	0.5	Positive		x
12	m	72	Negative	5.5	Negative		x
21	m	90	Negative	3.5	Negative		
22	f	58	Negative	1.5	Positive		

23	f	70	Positive	5	Negative		x
24	f	91	Negative	4	Negative		
25	m	83	Negative	5	Negative		
26	f	54	Negative	3	Negative	x	
27	m	80	Positive	5	Negative		x
28	f	54	Positive	3	Negative		
29	f	78	Positive	5.5	Positive		
30	m	69	Positive	7.5	Negative		x
31	m	73	Positive	3	Positive		

Figure legend

Figure 1. RNAseq-based transcriptomic analysis of cancer-associated stroma and matched normal stroma from 20 cases of cSCC. a) Principal component analysis (PCA) of all CAS and normal stromal samples. Blue: CAS, red: normal stroma. b) Volcano plot highlighting significantly differentially expressed genes in CAS compared to normal stroma, using fold change >2 and p-value < 0.01 (FDR<0.041910) as cut-off values. Significantly up-regulated genes are red, down-regulated ones are shown in blue. c) Heatmap of significantly differentially expressed genes in association with top 6 GO clusters. The table gives information on the different color-coded clusters. d and e) Hypergeometric overrepresentation of the biological processes associated with the most strongly up- (d) and down-regulated (e) genes in CAS compared to normal stroma.
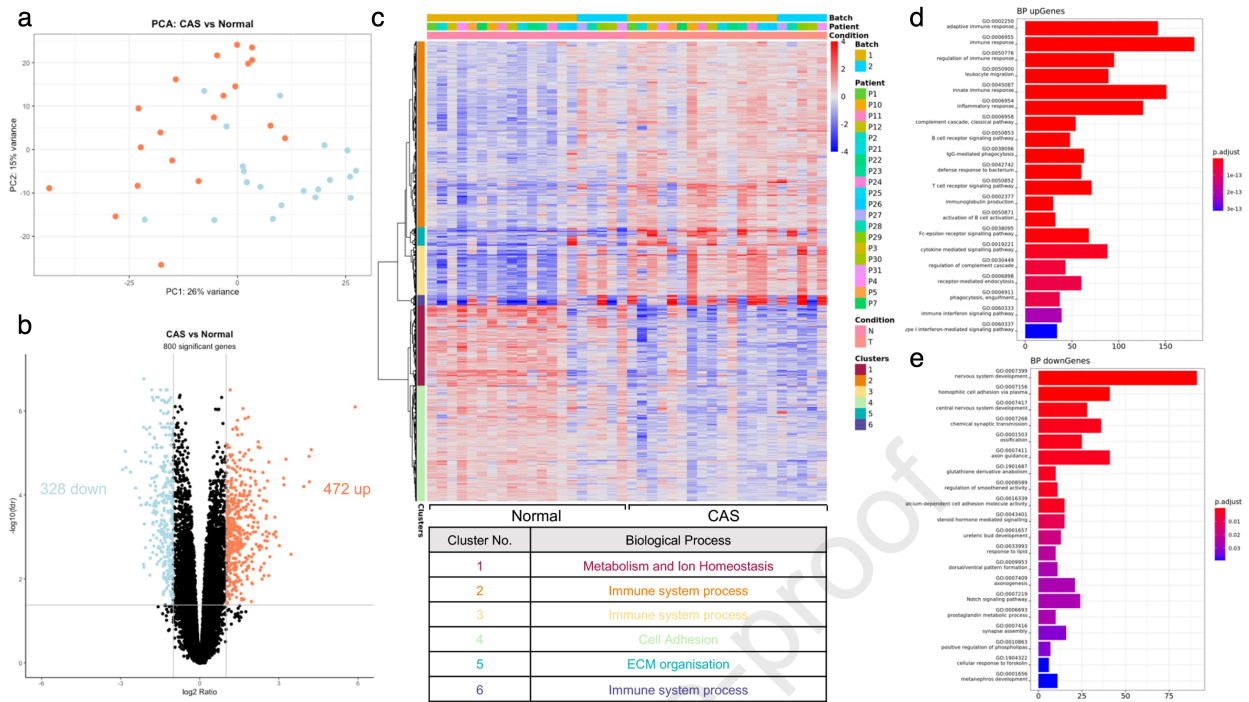
Figure 2. Validation of significantly differentially expressed genes in CAS vs normal

stroma of cSCC. (a, c, e, g, i, k, m) expression values of indicated genes in normal stroma and

CAS as determined by RNAseq. (b, d, f, h, j, l, n) expression values of indicated genes in normal

stroma and CAS as determined by RT-qPCR (n = 6 cases). P-values for RT-qPCR data are two-

tailed and were calculated using paired student's T-tests, with following categories: * = p<0.05,
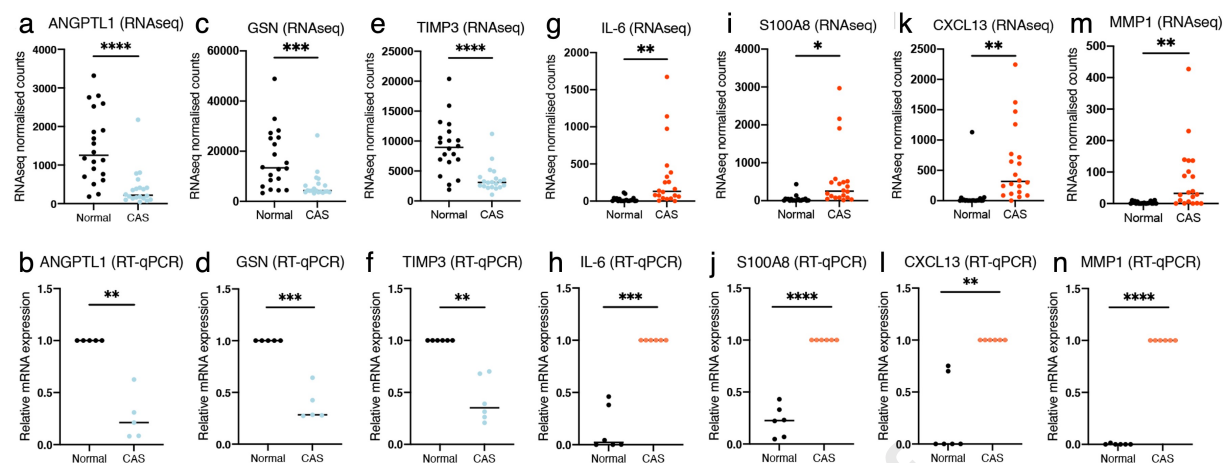
** = p<0.01, ***= p<0.001, **** = p<0.0001.

Figure 3. **Analysis of CAS vs normal stroma of cSCC**. a and b) GSEA of a) KEGG and b)

REACTOME pathways in CAS versus normal stroma. c) Stromal cell deconvolution using MCP-

counter. Y-axis shows fraction of the total cells, X-axis indicates the samples, where T = CAS

and N = normal. d) Predicted proportion of immune-related cells as determined by GEDIT

deconvolution. e) Predicted proportion of immune-related cells as determined by CIBERSORTx

deconvolution. f) Pair-normalized RNAseq counts of genes associated with immune modules in

CAS compared to normal. Shown are all individual values, their mean and SEM. All p-values are

two-tailed and were calculated using paired student's T-test, with following categories: * =

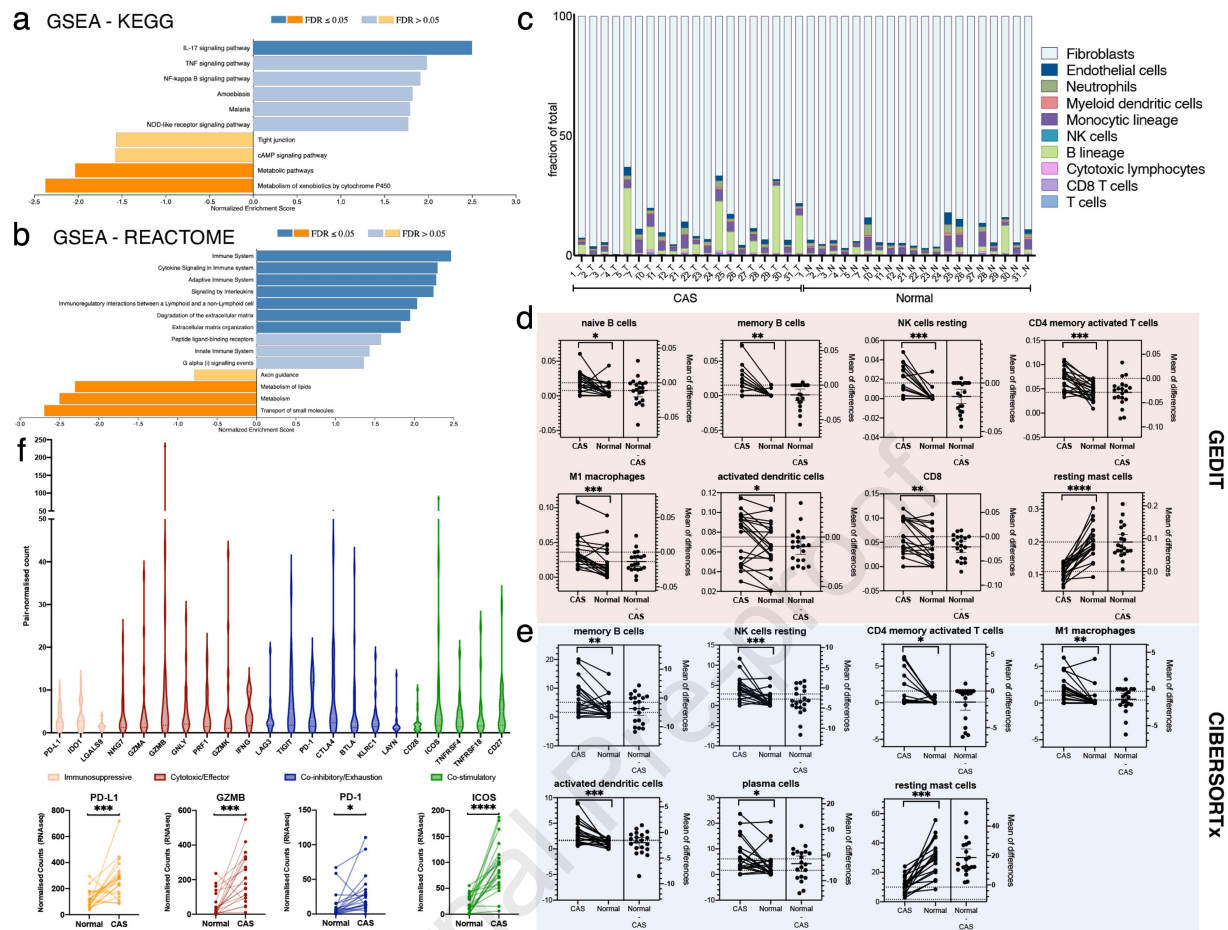p<0.05, ** = p<0.01, ***= p<0.001, **** = p<0.0001.

Figure 4. **Immunohistochemical analysis of the cellular composition in CAS vs normal**

stroma. Primary antibodies: CD4, CD8, CD138, CD20, CD 68, PD-1 and CD117. A

hematoxylin eosin (HE) picture with scale bar (1 mm) is added for comparison. The triangles

indicate the tumor islands. Magnification 200x.
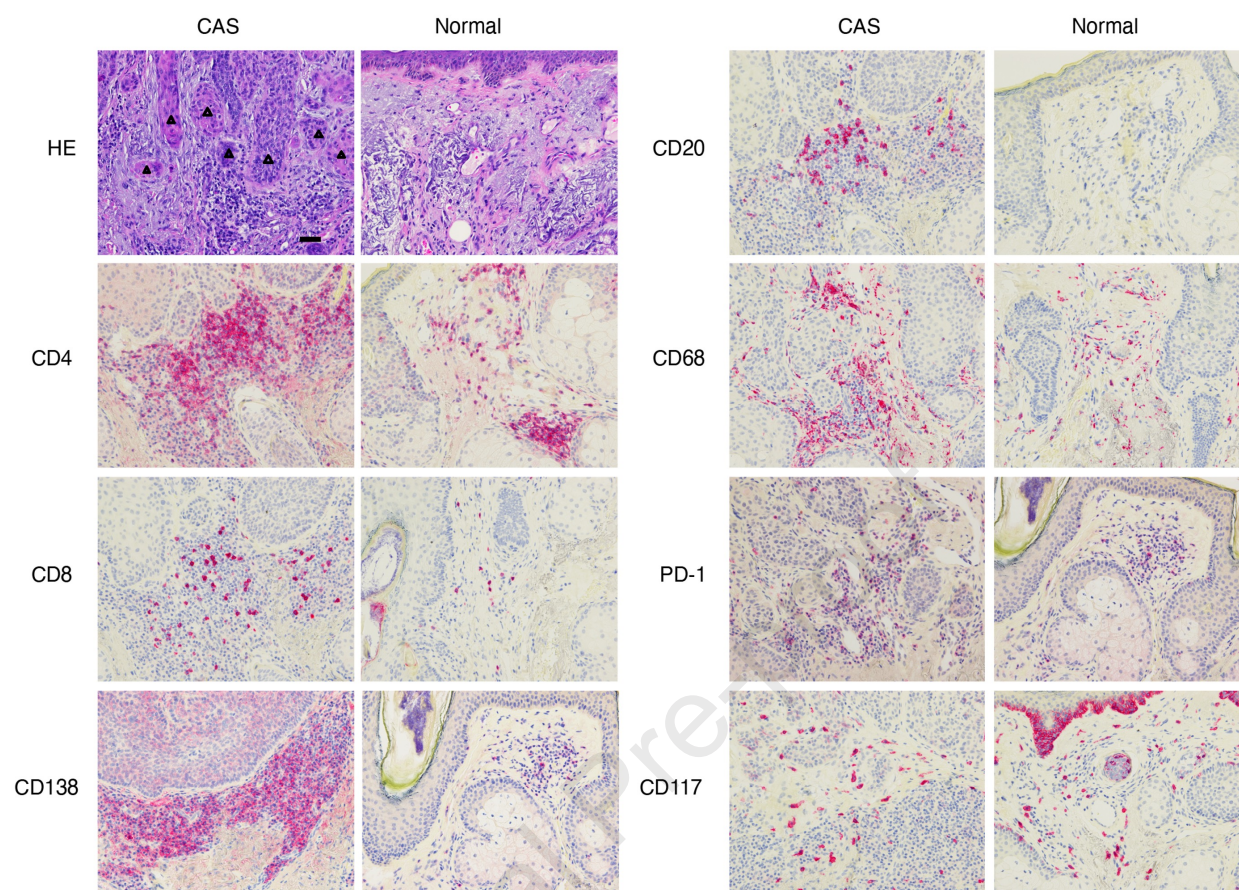
Figure 5. **Analysis of CAS in cases with and without PNI**. a) Volcano plot highlighting

significantly differentially expressed genes (p-value <0.05 , FC >2) (up-regulated in red, down-

regulated in blue. b) Heatmap of significantly differentially expressed genes in association with

top 6 GO clusters. c) Quantification of individual cell phenotype per ROI summarized per case

d) UMAP clustering of stromal cells from all samples. e) Heatmap of cell phenotype for each

cluster. f) Heatmap according to key cell types. g) Signal distribution of the top 25% of IL-17A

signal across cell phenotype (top) and cell type (bottom). h) Confirmation of co-expression in

key cell types with scale bar (10 µm). p-values are two-tailed and calculated using paired

student's T-tests. ** = $p<0.01$, ***= $p<0.001$, **** = $p<0.0001$, ns = not significant.

a

PCA: CAS vs Normal

b

CAS vs Normal
800 significant genes

328 down   472 up

c

Normal   CAS

Cluster No.	Biological Process
1	Metabolism and Ion Homeostasis
2	Immune system process
3	Immune system process
4	Cell Adhesion
5	ECM organisation
6	Immune system process

d

BP upGenes

e

BP downGenes

a ANGPTL1 (RNAseq)   c GSN (RNAseq)   e TIMP3 (RNAseq)   g IL-6 (RNAseq)   i S100A8 (RNAseq)   k CXCL13 (RNAseq)   m MMP1 (RNAseq)

b ANGPTL1 (RT-qPCR)   d GSN (RT-qPCR)   f TIMP3 (RT-qPCR)   h IL-6 (RT-qPCR)   j S100A8 (RT-qPCR)   l CXCL13 (RT-qPCR)   n MMP1 (RT-qPCR)

Supplementary Table S2: Overview of the number of significantly deregulated targets between normal stroma and CAS with respect to fold-change and p-value cut-offs. FDR = false discovery rate, FC = fold change.

	# of significants	FDR	FC ≥ 1	FC ≥ 1.5	FC ≥ 2	FC≥ 3	FC≥ 4	FC≥ 8	FC≥ 10
p<0.1	8318	0.228600	8318	2373	833	202	82	10	6
p<0.05	6839	0.139100	6839	2328	831	202	82	10	6
p<0.01	4538	0.041910	4538	2063	**800**	201	82	10	6
p<0.001	2514	0.007566	2514	1500	695	188	79	10	6
p<1e-04	1317	0.001444	1317	965	503	146	61	8	5
p<1e-05	661	0.000287	661	553	313	104	39	8	5

Supplementary Table S4: Overview of the number of significantly deregulated targets between CAS with and without PNI with respect to fold-change and p-value cut-offs. FDR = false discovery rate, FC = fold change.

|	# of significants	FDR	FC ≥ 1	FC ≥ 1.5	FC ≥ 2	FC≥ 3	FC≥ 4	FC≥ 8	FC≥ 10
p<0.1	3273	0.58160	3273	1272	427	123	54	9	7
p<0.05	1885	0.50450	1885	886	**340**	102	44	9	7
p<0.01	544	0.34880	544	327	144	47	22	7	6
p<0.001	67	0.27210	67	53	34	18	7	4	3
p<1e-04	9	0.19320	9	9	7	4	4	3	2
p<1e-05	1	0.07901	1	1	1	1	1	1	0

Supplementary Table S5: Detailed information on quantity and quality of RNA samples isolated from all cases used in this study.

| Case # (n=20)	CAS		Normal	
	conc. (pg/uL)	DV200	conc. (pg/uL)	DV200
1	15400	60.79	1290	65.99
2	17900	82.57	1040	72.2
3	14700	71.81	1050	69.22
4	13000	74.41	531	62.58
5	3750	72.55	3270	75.22
7	2040	68.73	1320	72.95
10	5820	77.59	2230	76.47
11	3890	65.13	1110	70.28
12	4170	78.33	539	64.27
21	1890	72.96	616	64.7
22	2040	76.86	835	59.4
23	1360	77.25	1060	69.18
24	2280	72.44	1040	67.6
25	4820	75.18	1080	54.98
26	5500	71.42	7480	70.41
27	5630	61.12	966	56.16
28	1990	54.91	917	57.35
29	21000	84.43	1690	69.85
30	2400	72.61	2230	64.29
31	1920	72.99	645	70.32

Supplementary Table S6: List of Taqman primers used for RT-qPCR in this study.

Gene target	Amplicon length (nt)	Taqman® Assay ID (ThermoFisher)
ANGPTL1	74	Hs00907665_m1
GSN	58	Hs00609272_m1
TIMP3	59	Hs00165949_m1
IL-6	60	Hs00985638_g1
S100A8	89	Hs05019740_g1
CXCL13	70	Hs00757930_m1
MMP1	64	Hs00899658_m1
GAPDH	58	Hs03929097_g1
B2M	64	Hs00187842_m1
PPIA	61	Hs01565699_g1

a

b

c

d

e

f
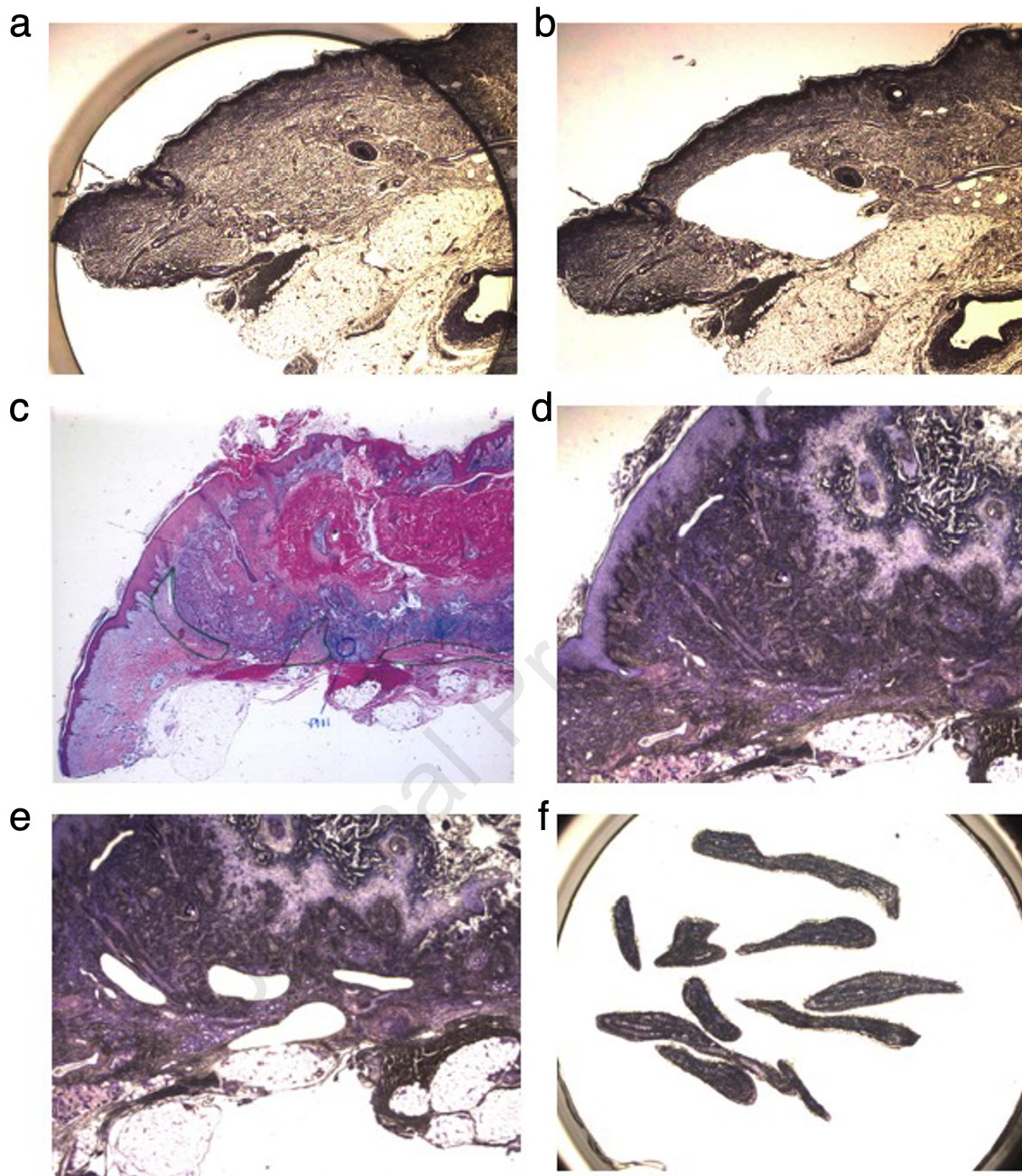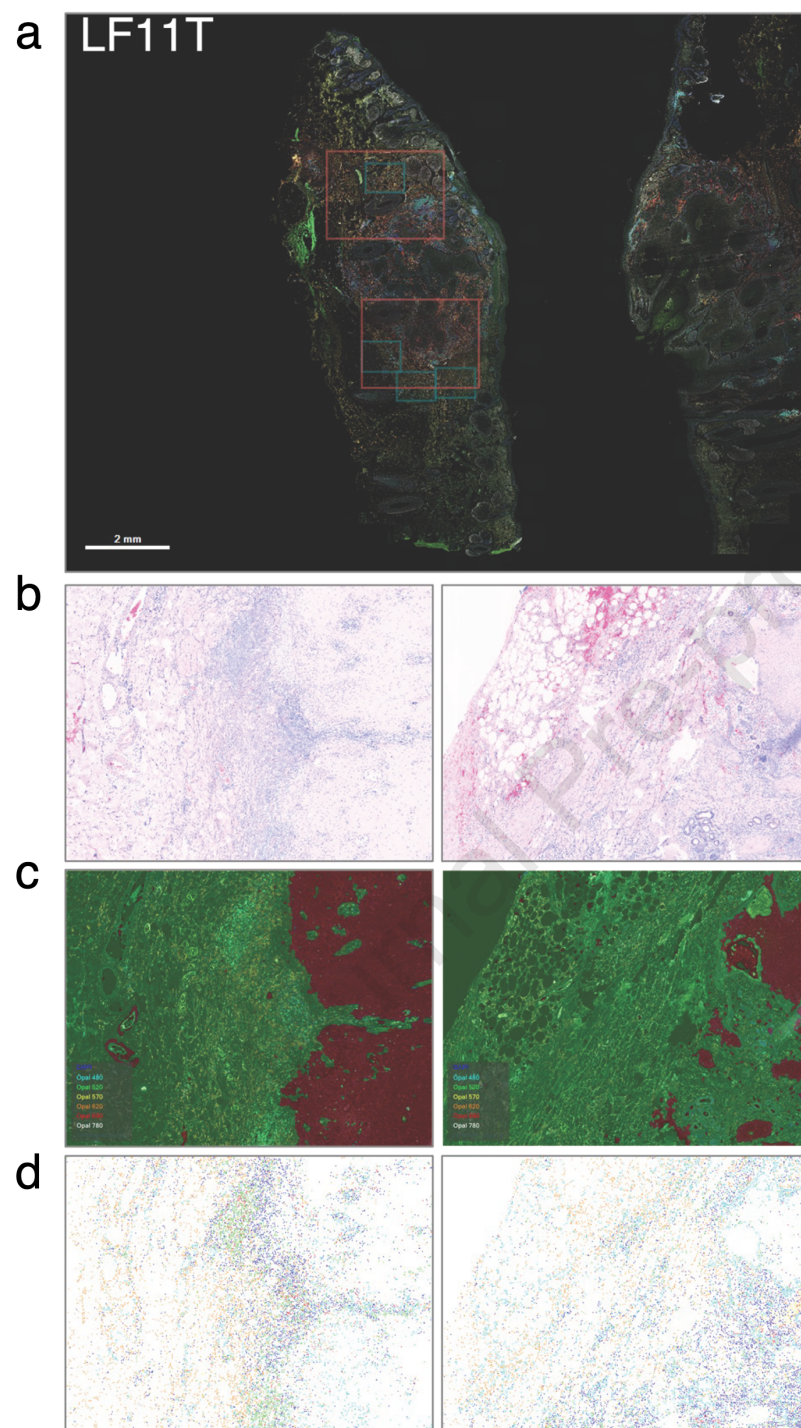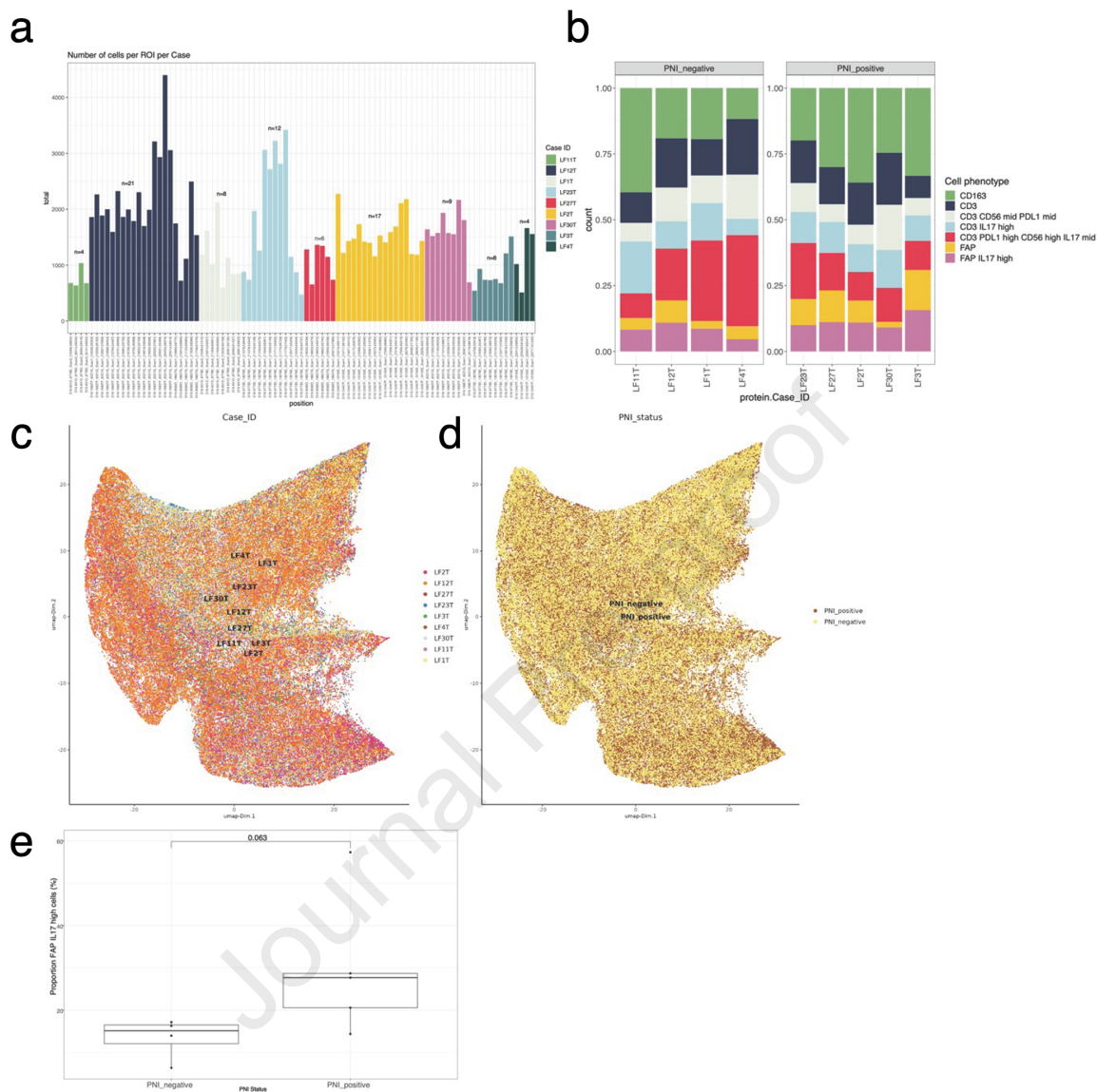
Supplementary Methods

Laser-capture microdissection.

To avoid sampling bias, isolation was performed blinded with regards to PNI status. Areas for dissection were reviewed by a dermatopathologist (LF). CAS was isolated according to the following criteria: stroma directly adjacent to the tumor up to max 3 mm distance from the tumor border. Matched normal stroma was isolated from regions of the dermis that presented no obvious alterations and were at least 4 mm away from the tumor, in accordance with established procedures (Finak et al. 2008). Isolation of areas of interest was verified by microscopic examination of the LCM cap as well as the excised region after microdissection (Supplementary Figure S1).

Multiplex immunohistochemistry. 9 cSCC cases were selected for additional analysis with multiplex immunohistochemistry, 5 presenting with PNI and 4 without. 4 μm sections of FFPE tissue were mounted on superfrost slides and deparaffinized using BOND Dewax Solution. Immunofluorescent signal was visualized using Opal kit with dyes 480, 520, 570, 620, 690, 780 counterstained with DAPI. Fluorescence exposure times were manually optimized for each slide prior to image acquisition.

As mentioned, whole slide scans were visualised and annotated using Phenochart (Akoya Biosciences). First, representative 2x2 ROI were selected and used to train an algorithm capable of tissue segmentation, cell segmentation and cell phenotyping (Supplementary Figure S2). Next, multiple 1x1 ROIs, corresponding to regions of CAS isolated with LCM, were selected per tissue section for InForm batch analysis, incorporating the manually trained segmentation algorithm.

Spatial expression analysis using Giotto (version 2.0.0.957) was performed as follows. Cell segmentation data output from inForm image processing, was read to the function *createGiottoObject*. Additional metadata including Case ID, ROI annotation ID and PNI status were added to the giotto object thus were available for data visualization. The giotto object was further filtered using *filterGiotto* with the following argument thresholds: *expression_threshold =1, feat_det_in_min_cells =3, min_det_feats_per_cell =1*. Next, normalization was applied using *normalizeGiotto* with the default scalefactor of 6000 and scale_cells = TRUE. Dimension reduction was performed using *runPCA* including CD3, CD163, CD56, FAP, IL-17A and PD-L1 as *feats_to_use* and *expression_values* was set to *"normalized"*. A UMAP plot was then used to visualize clustering of individual cells from all samples according to expression similarities. Individual clusters were identified applying *createNearestNetwork* (k=50) in combination with *doLeidenCluster* (resolution = 0.4). Finally, *plotMetaDataHeatmap* with selected features was used to visualize characteristic cell phenotypes of each cluster generated. Clusters were manually annotated with a phenotype description and subsequently merged according to key cell types to achieve clear visualization of marker co-expression. The top 25% of IL-17A signal was annotated as IL-17 high and expression distribution across previously identified cluster phenotypes was analyzed to identify contributing cell types. Metadata of individual cells used in this analysis is available in Supplementary Table S7.

Supplementary Table Legends:

Supplementary Table S1: Complete list of differentially expressed genes in CAS compared to matched normal stroma.

Supplementary Table S3: Complete list of differentially expressed genes in CAS from cases presenting with vs without PNI.

Supplementary Table S7: Single cell metadata acquired through multiplex IHC.

Supplementary Figure Legends:

Supplementary Figure S1: Selective isolation of regions of interest from clinical cases of cSCC. Representative images of tissue a) before microdissection and b) after microdissection to validate the isolation of the selected area. c-f) Representative images of a second case of cSCC presenting with PNI. c) H&E overview of tissue sections annotated with regions of CAS to be isolated and identification of PNI. d) tissue section stained with cresyl violet before and e) after microdissection. f) validation of isolation of specific sections of CAS.

Supplementary Figure S2: Representative images of ROI selected to train tissue and cell segmentation algorithms using inForm software. a) Visualization of ROI in phenochart. Red ROI (2x2) indicate regions used to train tissue and cell segmentation algorithms. Blue ROI (1x1) indicate ROI input for batch analysis with the newly trained segmentation algorithm.Red Training ROI were not included in final spatial expression analysis. b) H&E presentation view of ROI. c) Representative results of tissue segmentation training (red is

tumour, green is stroma). d) Representative results of individual cell segmentation and

phenotyping.

Supplementary Figure S3: Summary of cell heterogeneity. a) Barchart of cell count per

ROI per case. b) Stacked barchart of cell phenotype normalized per patient sample. c) UMAP

of all cells colored by case confirming patient heterogeneity. d) UMAP of all cells colored by

PNI status. e) Boxplot comparing proportion of FAP IL17 high cells in PNI negative and PNI

positive corresponding to Fig. 5g (top).